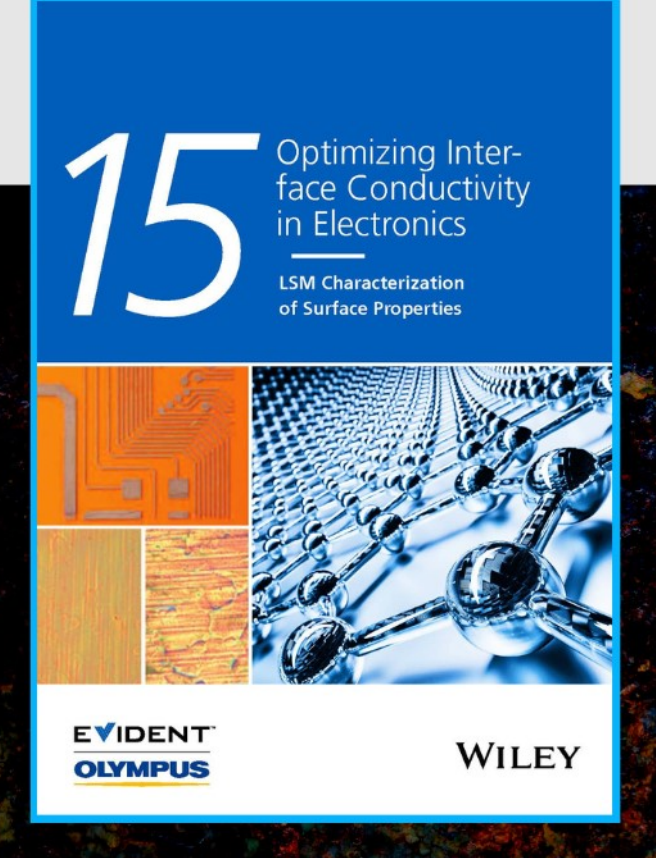


Optimizing Interface Conductivity in Electronics



The latest eBook from Advanced Optical Metrology. Download for free.

Surface roughness is a key parameter for judging the performance of a given material's surface quality for its electronic application. A powerful tool to measure surface roughness is 3D laser scanning confocal microscopy (LSM), which will allow you to assess roughness and compare production and finishing methods, and improve these methods based on mathematical models.

Focus on creating high-conductivity electronic devices with minimal power loss using laser scanning microscopy is an effective tool to discern a variety of roughness parameters.



WILEY

Check for updates

Ionic Liquid-Mediated Scanning Probe Electro-Oxidative Lithography as a Novel Tool for Engineering Functional Oxide Micro- and Nano-Architectures

Zixuan Li, Jerzy T. Sadowski, Andrei Dolocan, and Filippo Mangolini*

Functional oxides have extensively been investigated as a promising class of materials in a broad range of innovative applications. Harnessing the novel properties of functional oxides in micro- to nano-scale applications hinges on establishing advanced fabrication and manufacturing techniques able to synthesize these materials in an accurate and reliable manner. Oxidative scanning probe lithography (o-SPL), an atomic force microscopy (AFM) technique based on anodic oxidation at the water meniscus formed at the tip/substrate contact, not only combines the advantages of both "top-down" and "bottom-up" fabrication approaches, but also offers the possibility of fabricating oxide nanomaterials with high patterning accuracy. While the use of self-assembled monolayers (SAMs) broadened the application of o-SPL, significant challenges have emerged owing to the relatively limited number of SAM/solid surface combinations that can be employed for o-SPL, which constrains the ability to control the chemistry and structure of oxides formed by o-SPL. In this work, a new o-SPL technique that utilizes room-temperature ionic liquids (RTILs) as the functionalizing material to mediate the electrochemistry at AFM tip/substrate contacts is reported. The results show that the new IL-mediated o-SPL (IL-o-SPL) approach allows sub-100 nm oxide features to be patterned on a model solid surface, namely steel, with an initiation voltage as low as -2 V. Moreover, this approach enables high tunability of both the chemical state and morphology of the patterned iron oxide structures. Owing to the high chemical compatibility of ILs, which derives from the possibility of synthesizing ILs able to adsorb on a wide variety of solid surfaces, IL-o-SPL can be extended to other material surfaces and provide the opportunity to accurately tailor the chemistry, morphology, and electronic properties within nanoscale domains, thus opening new pathways to the development of novel micro- and nano-architectures for advanced integrated devices.

1. Introduction

Functional oxide materials have been gaining increasing interest over the last few decades for their unique and highly tunable physico-chemical properties.[1-3] The ability of these materials to exhibit a wide range of properties originates from the strong dependence of their electronic band structure on the oxides' structure and chemistry.[4,5] Even more importantly, functional oxides are usually categorized as having strongly correlated magnetic and electronic states, which make them completely different from materials whose properties can be described using free electron models.[6-9] Given the possibility of controlling the electronic and magnetic properties by modifying the structure, chemistry, and subsequent phase transitions of functional oxides, these materials have emerged as candidates for the design and development of integrated devices.[7,6,10-11]

The progressive optimization and advancement of micro- to nano-scale manufacturing and fabrication methods offer new possibilities for the technological exploitation of functional oxides, while also allowing for the identification of fundamentally new properties and functionalities originating from the confined dimension of nanomaterials. [12–16] As an example, iron oxides, mostly considered as a class of widely available, inexpensive, and benign oxide materials, have attracted

Z. Li, A. Dolocan, F. Mangolini
Texas Materials Institute
The University of Texas at Austin
Austin, TX 78712, USA
E-mail: filippo.mangolini@austin.utexas.edu
Z. Li
Materials Science and Engineering Program
The University of Texas at Austin
Austin, TX 78712, USA

The ORCID identification number(s) for the author(s) of this article can be found under https://doi.org/10.1002/adfm.202306660

DOI: 10.1002/adfm.202306660

Laurence Light Source Division
Lawrence Berkeley National Laboratory
Berkeley, CA 94720, USA
J. T. Sadowski
Center for Functional Nanomaterials
Brookhaven National Laboratory
Upton, NY 11973, USA
F. Mangolini
Walker Department of Mechanical Engineering
The University of Texas at Austin
Austin, TX 78712, USA

www.advancedsciencenews.com



www.afm-journal.de

considerable attention in catalysis, [17-19] sensing, [20-23] material separation,[24-26] and magnetic data storage[27-29] when used in various nanostructured forms. To control the structure and. hence, the physico-chemical properties of functional oxides, intricate procedures have been developed to synthesize nanostructures and assemble them into complex architectures.^[1,30–32] While the preparation of these materials has heavily relied on solution-based chemical methods,[33-35] harnessing their novel properties in new functional devices requires the integration of oxide nanomaterials into architectures of greater complexity. This is generally accomplished by two assembly methods, i.e., the topdown and bottom-up approaches. The combination of these two approaches can enable the assembly of small functional building blocks into larger arrangements while patterning the structure into predefined positions.[36,37] However, using these combined methods to fabricate micro- to nano-structures with high precision and site specificity is technically demanding, often requiring multi-step procedures involving advanced lithographic techniques and strictly controlled processing conditions. In all these processing approaches, chemical compatibility and interfacial effects deriving from the coupling of chemically different compounds pose significant challenges. Despite some success in building complex nanoarchitecture, [38-40] the development of nanopatterned functional oxide materials for next-generation applications hinges on establishing novel, cost- and time-effective fabrication approaches.

Since the late 1980s, scanning probe lithography (SPL) has emerged as a class of fabrication techniques that combines high positional selectivity and great amenability regarding chemical functionalization, while overcoming some of the limitations of other advanced lithographic techniques. For example, many SPL techniques can operate at room temperature and in atmospheric environment and do not require the use of photoresists or wet chemical etching processes.^[41] The versatility of atomic force microscopy (AFM) enables a variety of approaches to modify surfaces and manipulate small-scale features based on the highly confined AFM tip/substrate interactions.[42-46] Among them, oxidative SPL (o-SPL) has become a widely used technique for micro- to nano-scale patterning and device fabrication in academic research, supporting not only single-step local oxidation of materials, but also more complex procedures for its great compatibility with other lithographic techniques.^[41]

O-SPL is based on the local anodic oxidation confined by the nanoscale water meniscus formed at the AFM tip/substrate contact, where the biased AFM tip acts as the cathode to initiate the oxidation reaction at the counter surface (anode), while the water meniscus provides the electrolytic environment for the electrochemical reaction. The oxidation process is described by two half-cell reactions, one on the anode surface where the substrate material (metals or semiconductors) becomes oxidized (Reaction I), and the other one at the AFM tip where hydrogen evolution (Reaction II) occurs:^[47]

$$M + nH_2O \rightarrow MO_n + 2nH^+ + 2ne^-$$
 (1)

$$2H^{+}(aq) + 2e^{-} \rightarrow H_{2}$$
 (2)

Since only the substrate material and water are involved in the nano-cell reactions, this approach can theoretically be car-

Adv. Funct. Mater. 2023, 2306660

ried out on bare surfaces. Nonetheless, it is practically challenging to maintain distance between the electrodes while stabilizing the water meniscus at the tip/substrate contact. For this reason. o-SPL on unfunctionalized surfaces is mostly limited to siliconbased patterning. [48-50] The introduction of self-assembled monolayers (SAMs) on surfaces as resist layers is therefore considered a major breakthrough as they can separate the anode and cathode and stabilize the meniscus during patterning, hence providing better control and improving writing efficacy.[51,52] The addition of SAMs also allows for the application of o-SPL on a wider range of materials, including III-V semiconductors and several metals. Notably, this approach was successfully employed for the formation of indium tin oxide. [53,54] While organofunctional silanes, such as octadecyltrichlorosilane (OTS), are predominantly used to form SAMs for o-SPL, the selection of functionalizing materials is still too limited to ensure the applicability of this method to a broad range of semiconductors and metallic materials. On the other hand, the high voltages required for patterning on organosilane-functionalized surfaces pose additional challenges to the oxide fabrication process. A literature survey indicated that a minimum voltage of -5 V is generally needed for oxidizing the underlying substrate, while in some cases it can be up to -30 V.[41,47] Such large negative voltages can not only lead to severe surface damage but also make it extremely difficult to modulate oxidation through nano-cell electrochemical reactions at the tip/substrate contact, especially for materials with several oxidation states that require accurate tuning. New solutions for surface functionalization in SAM-based o-SPL ought to address these problems.

Among potential candidate functionalizing materials for o-SPL, room-temperature ionic liquids (RTILs)^[55] are particularly attractive for several reasons. First, the ionic nature of RTILs ensures that they can adsorb on virtually all polar surfaces, including most transition metals and metal oxides as well as various semiconductors. [56-60] Second, RTILs can form well-defined electrical double-layer (EDL) structures at electrified interfaces. [61] These EDL structures can not only provide good interface stability at the electrode surface but also enables efficient transfer of electrons and ions - a critical requisite for the electrochemical reactions for o-SPL.^[61] The unique ability of RTILs to form dense EDLs together with their wide electrochemical windows^[62] have already resulted in significant interest in exploiting RTILs as electrolytes for renewable energy storage devices. [61,63] RTILs respond to electric fields by creating current through the translational motion of ions, while other motions, such as ion rotation and vibration, contribute to the IL's polarization.^[62] These attributes of RTILs can allow for more efficient electron transfer for o-SPL than non-ionic SAMs, therefore reducing the threshold voltage to initiate oxidation. Moreover, the high electrochemical stability of RTILs not only ensures their durability as resist materials in electrified environments, but also prevents the introduction of unwanted contaminants in oxide materials from the decomposition of the resist layer.

Here, we demonstrate, for the first time, an o-SPL approach that uses an AFM tip to induce local oxidation on steel surfaces functionalized with an RTIL, i.e., trihexyltetradecylphosphonium bis(2-ethylhexyl)phosphate ([P_{6,6,6,14}][DEHP], see **Figure 1c**). The results show that IL-mediated o-SPL (IL-o-SPL) could achieve patterning of sub-100 nm features, with an initiation voltage as

16163028, 0, Downloaded from https://onlinelibrary.wiley.com/doi/10.1002/adfm.20230660 by University Of Texas Libraries, Wiley Online Library on [26/07/2023]. See the Terms and Conditions (https://onlinelibrary.wiley.com/rems

-and-conditions) on Wiley Online Library for rules of use; OA articles are governed by the applicable Creative Commons

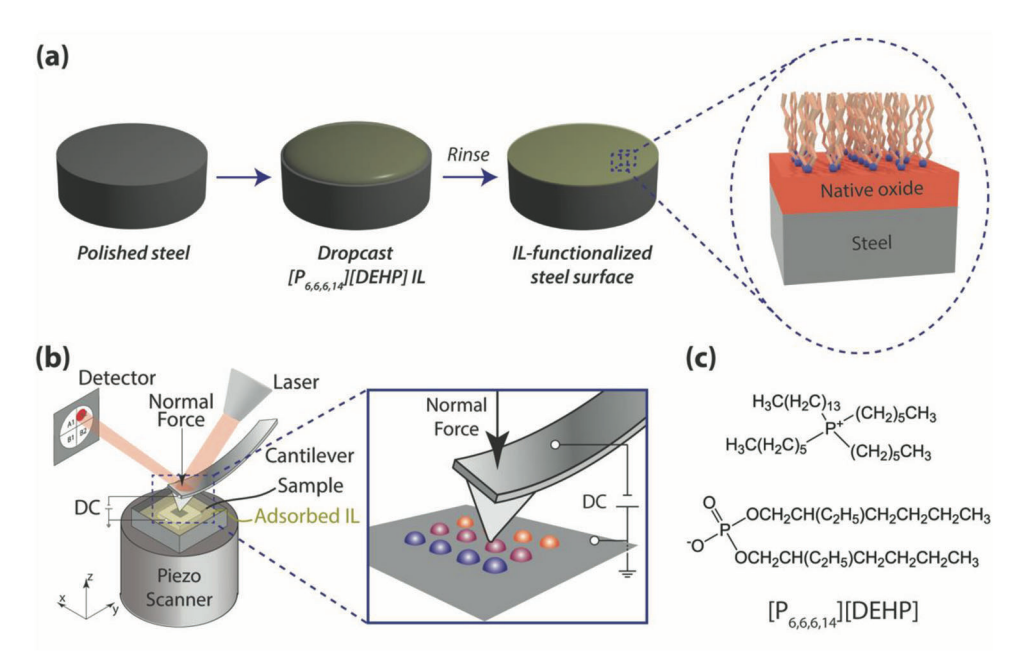


Figure 1. a) Procedure for preparing $[P_{6,6,6,14}][DEHP]$ -functionalized steel substrates. b) AFM experimental setup for o-SPL on an IL-functionalized surface. The electric loop connected with the AFM setup is shown with a voltage applied across the tip/substrate interface while the substrate is grounded. c) Chemical structure of $[P_{6,6,6,14}][DEHP]$.

low as -2 V. The outcomes of surface analyses, including Xray photoemission electron microscopy (X-PEEM), time-of-flight secondary ion mass spectrometry (ToF-SIMS), and AFM imaging, reveal the dependence of oxide morphology and chemistry on several experimental parameters, i.e., the applied voltage, relative humidity (RH), and atmospheric composition during the oxidation process. In particular, the oxide layer morphology (thin film/island mode growth) was found to be dependent on the current density across the water bridge at the AFM tip/substrate contact. Additionally, the Fe³⁺/Fe²⁺ ratio in the oxide layer could be tuned by varying the tip voltage or O₂ partial pressure in the environment. Further analyses by Kelvin probe force microscopy (KPFM) and low energy electron microscopy (LEEM) indicated that the surface polarization of IL-o-SPL oxide thin films differs from the native oxide on steel as a result of multiple factors, including the change in structural ordering of the SAM-substrate complex. These findings can pave the way for creating microto nano-scale domains with controlled morphological, chemical, and electronic properties. Although this work mainly focuses on the [P_{6,6,6,14}][DEHP]-steel pair, the notion of using o-SPL on ILfunctionalized materials can be extended to numerous combinations including many novel functional systems, leading to virtually endless possibilities for building oxide-based nanoarchitectures and nanodevices.

2. Results and Discussion

2.1. Morphology of IL-o-SPL Oxides

IL-o-SPL experiments were carried out on $[P_{6,6,6,14}][DEHP]$ -functionalized 52100 steel surfaces (see schematic of the preparation procedure of the substrate in Figure 1a. Note: while the results presented below were obtained using steel as substrate

material, similar experiments were performed using silicon wafers to demonstrate the applicability of IL-o-SPL to other substrate materials, see Figure S1 in the Supporting Information). The driving force for the electrochemical reaction in the nanocell (Figure 1b), i.e., the bias voltage applied to the conductive AFM tip, was found to significantly impact the morphology and surface chemistry of the oxide films formed as a result of the contact-point oxidation at the [P_{6.6.6.14}][DEHP]-functionalized surface. The $5 \times 5 \mu m^2$ topographic images displayed in Figure 2a were acquired after growing oxide films in the central $2 \times 2 \mu m^2$ area in ambient air (≈50% RH). The film morphology considerably changed with the tip bias voltage: with a more negative voltage, the film not only became drastically thicker (Figure 2b), but also consisted of larger "islands" (Figure 2a) and exhibited less defined boundaries. These changes are attributed to the effect of varying the current density across the tip/substrate contact as well as electrowetting, both induced by changing applied voltage. In fact, the increase in feature size with current density has been well documented in traditional electrochemical setups where aqueous electrolytes are used. [64,65] Additionally, a more negative applied voltage can lead to a decrease in contact angle and an increase in the base area of the meniscus at the tip/substrate contact as a result of electrowetting, [66] which in turn can also affect the size of the surface nuclei forming during the process. It has to be highlighted that no oxide films could be grown under the same experimental conditions but in the absence of the IL surface functionalization (Figure S2, Supporting Information).

It is also worth noting that the oxidation could be initiated at a tip bias as low as -2 V, resulting in an average film thickness of 3.3 nm as shown in Figure 2b. As the tip voltage becomes more negative, the film became thicker. At -5 V, the film thickness was \approx 81 nm. Figure 2b also indicates an increase in roughness of the

16163028,0, Downloaded from https://onlinelibrary.wilej.co.ord/oi/10.1002/adfm.202306660 by University Of Texas Libraries, Wiley Online Library on [26/07/2023], See the Terms and Conditions (https://onlinelibrary.vilej.co.or/rems-and-conditions) on Wiley Online Library for rules of use; OA archies are governed by the applicable Creative Commons Licensed

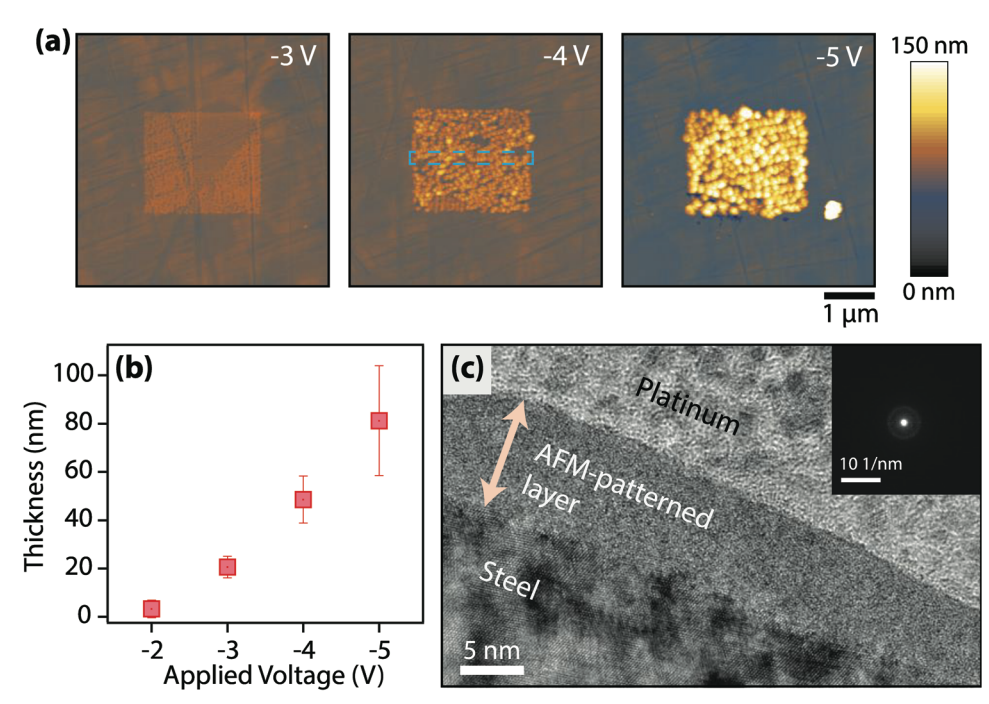


Figure 2. a) $5 \times 5 \,\mu\text{m}^2$ AFM topographic images of iron oxide thin films grown in the central $2 \times 2 \,\mu\text{m}^2$ area by IL-o-SPL. The substrate is a $[P_{6,6,6,14}][\text{DEHP}]$ -functionalized ASTM 52100 steel surface. The tip bias was -3 V, -4 V, and -5 V (from left to right). All experiments were performed in an ambient environment (RH \approx 50%). b) Dependence of oxide thickness on the applied voltage. The error bars reflect the film roughness as shown in (a). c) Transmission electron microscopy (TEM) imaging on the cross-section at the oxide/steel interface, which is obtained from an oxide film formed at -4 V. The blue dashed rectangle shown in the oxide area in (a) highlights the sampled area. The inset shows the electron diffraction pattern obtained in the oxide area.

oxide film surface, demonstrated by the widening error bar as the bias becomes more negative. This roughness change with bias voltage is due to the different morphology of the grown oxide as larger islands are formed at higher voltages (Figure 2a).

While the morphology of the oxide films was affected by the bias voltage applied to the conducting AFM tip, their structure, which was evaluated by TEM, did not change with the patterning conditions. Figure 2c displays a typical cross-sectional TEM image of a film grown with a tip bias of -4 V. A well-defined, sharp interface between the iron oxide and the underlying steel substrate was observed. Compared to the steel layer where longrange order is preserved, the atoms in the oxide layer are not organized in any ordered pattern. Further proof of a lack of extended crystallinity is shown in the inset image where the nanobeam electron diffraction pattern shows only a bright center and two broad hazy concentric bands. The formation of a metastable amorphous structure is the result of the non-equilibrium conditions developing during the local oxidative process induced by the tip-enhanced electric field.

2.2. Surface Chemistry of IL-o-SPL Oxides

The change in morphology of the patterned oxides resulted in variations in the yield of fragments detected by ToF-SIMS. **Figure 3**a displays a high-lateral-resolution ToF-SIMS chemical depth profile of secondary FeO $^-$ ions acquired on a $[P_{6,6,6,14}][DEHP]$ -functionalized steel surface where IL-o-SPL experiments were performed at different tip voltages. The FeO $^-$

yield is much higher on the patterned areas than on the asprepared surface, where a thin native oxide layer is present. This is due to the increased oxide thickness as indicated by topographic AFM results (Figure 2). The ToF-SIMS chemical map in Figure 3a also indicates a subtle change from homogeneous to island-like lateral distribution as the tip bias was changed from -3 V to -5 V, while the FeO $^-$ yield did not significantly change. This can be attributed to the different morphology of the films, since, as indicated by Figure 2a, a more negative the tip voltage results in larger islands and rougher films.

A similar transition from laterally homogeneous thin film to islands was observed when analyzing ToF-SIMS chemical maps of other ions acquired on films formed at different voltages. Figure 3b presents close-up views over the lateral (*x*-*γ* plane) and vertical (*x*-*z* plane) maps of FeO⁻, FeO₂⁻, and FeOH⁻ obtained upon analyzing IL-o-SPL films formed at −4 V and −5 V. The in-plane (*x*-*γ*) variation in the yield of molecular fragments was matched by their vertical (*x*-*z* plane) yield distribution: a transition from continuous to striped distribution in ion yield was observed upon changing the tip voltage from −4 V to −5 V. The vertical (*x*-*z* plane) maps cover only a small fraction of the oxide film thicknesses (over a few Angstroms). The decay of oxide species in *z*-direction is due to depletion of Cs during data acquisition, as Cs enhances the ionization probability of negative species including those in Figure 3b.^[67]

The changes in oxide film morphology were also substantiated by SEM analyses. The SEM micrographs shown in Figure 3c indicated that the oxide islands become larger as the voltage changed from -4 V to -5 V. Additionally, pits could be detected in some

16163028, 0, Downloaded from https://onlinelibrary.wiley.com/doi/10.1002/adfm.202306660 by University Of Texas Libraries, Wiley Online Library on [26/07/2023]. See the Terms and Conditions (https://onlinelibrary.wiley.com/term

-and-conditions) on Wiley Online Library for rules of use; OA articles are governed by the applicable Creative Commons

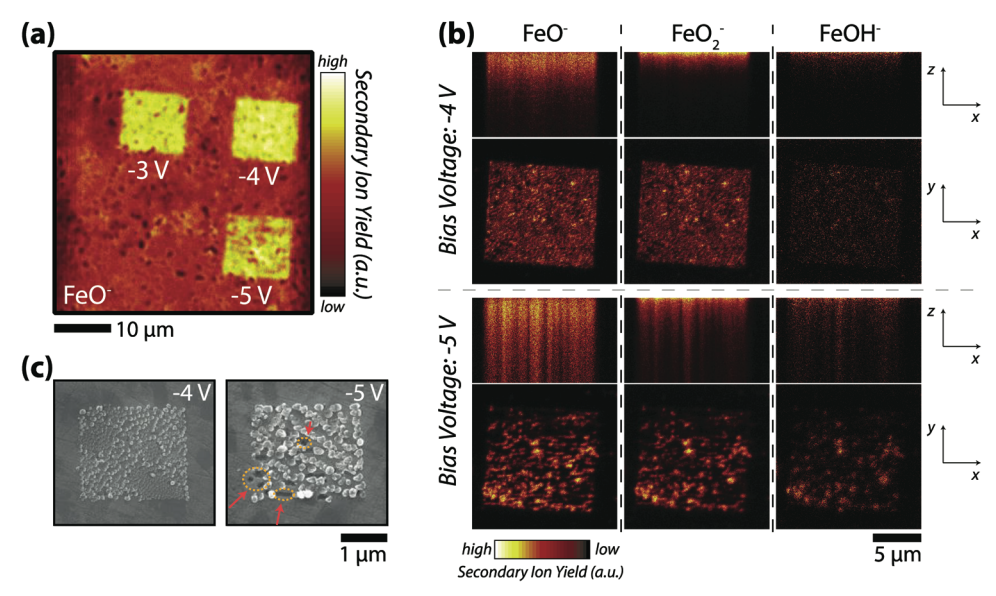


Figure 3. a) High-lateral-resolution ToF-SIMS chemical depth profile of secondary FeO⁻ ions acquired on $[P_{6,6,6,14}][DEHP]$ -functionalized steel over which IL-o-SPL experiments were carried out with different tip biases. b) Lateral and vertical chemical distributions (specified by Cartesian coordinates on the right) of FeO⁻, FeO₂⁻, and FeOH⁻ secondary ions determined by ToF-SIMS high-resolution imaging of a $[P_{6,6,6,14}][DEHP]$ -functionalized steel surface over which IL-o-SPL experiments were performed at -4 V and -5 V. The scale bar only refers to the lateral $(x \cdot y)$ dimensions. In vertical maps, z is on the order of a few Angstroms. c) Scanning electron microscopy (SEM) images of IL-o-SPL oxide films fabricated by different tip biases. Pits highlighted in the image on the right. All IL-o-SPL experiments were performed in an ambient environment (RH $\approx 50\%$).

locations of the films formed at -5 V (highlighted in Figure 3c, right). This can be attributed to the tip's high negative voltage, which causes the oxidation of subsurface iron due to the uneven surface conductivity. The resulting electron exchange in the near-surface region inside the steel leads to a second cathodic reaction on the steel surface, i.e., the reduction of oxygen in the water meniscus and the formation of OH- - a process similar to the mechanism that drives pitting corrosion.^[68] Because of the dissolution of iron and iron oxide in the pitted areas, portions of the [P_{6,6,6,14}][DEHP] SAM in those areas are desorbed. Overall, while the combination of AFM, SEM, and ToF-SIMS results reveal that all iron oxide films prepared in the present work form at randomly located nucleation sites followed by film growth, the transition from a thin-film morphology to an island morphology as the tip bias was changed from -4 V to -5 V provides evidence that the nucleation rate of the films strongly depends on and, thus, can be controlled by the applied tip voltage.

To further evaluate the surface chemistry of IL-o-SPL oxide layers, X-PEEM analyses were performed at the X-PEEM/LEEM endstation of the ESM (21-ID) beamline of the National Synchrotron Light Source II at Brookhaven National Laboratory. Figure 4a displays X-PEEM images of the oxide films acquired at a photon energy of 706.8 eV. The contrast in the X-PEEM images corresponds to differences in secondary electron yield. More specifically, a decrease in secondary electron yield was detected in the oxidized areas relative to the as-prepared surface. The acquisition of an X-PEEM image stack across a photon energy range between 701.8 eV and 729.0 eV allowed for the extraction of X-ray absorption near edge structure (XANES) spectra from regions of interest (ROIs). Figure 4b displays the iron 2p (Fe 2p) XANES spectra, which are the result of transitions of Fe 2p electrons to

higher unoccupied states. Specifically, due to spin-orbit splitting, the L₃ edge represents the transition of electrons from the 2p_{3/2} to the 3d orbital, whereas the L2 edge represents the transition from the 2p_{1/2} to the 3d orbital.^[69] Further energy split can be seen in the 2p_{3/2}-to-3d transitions as indicated by the doublet present at the L₃ edge. Due to the octahedral symmetry, which is the predominant coordination for Fe in FeO and Fe₂O₃,^[70] the transition peak (1) at \approx 706.6 eV represents the t_{2g} orbit and the peak (2) at \approx 708.0 eV represents the e_g orbit. [69] This Fe 3d orbit splitting originates from ligand field effects in the presence of Fe-centered octahedral complexes characterized by the hybridization of Fe 3d-O 2p orbitals, which gives rise to distinct lineshapes differentiating the iron oxidation states (Fe³⁺ and Fe²⁺).^[69,71,72] Typically, the L_3 edge of FeO features a single t_{2g} peak, while the L₃ edge of Fe₂O₃ has a well-defined doublet with a prominent e_g peak and a much weaker t_{2g} peak (reference spectra shown in Figure S3 in the Supporting Information). [73-75] Therefore, the relative contents of Fe³⁺ and Fe²⁺ of the IL-o-SPL oxide films can be estimated by performing linear combination fitting (LCF) using normalized reference spectra of FeO and Fe₂O₃. Figure 4cf show the fitting results of the L_3 edge of a $[P_{6,6,6,14}][DEHP]$ functionalized native oxide (IL-NO) area and oxide films formed by IL-o-SPL at -3 V, -4 V, and -5 V. The weighted percentage of the Fe₂O₃ spectrum increases as the applied tip voltage used in the IL-o-SPL process becomes more negative. The quantitative results of the LCF displayed in Figure 4g indicate that in IL-NO, the Fe³⁺ content is \approx 0.49, while in the IL-o-SPL oxide films, the Fe³⁺ content is higher and increases as the tip voltage becomes more negative, with the highest at ≈ 0.71 at -5 V. This dependence of the iron oxidation state on the tip bias suggests that a higher voltage difference at the tip/substrate contact favors the oxidation of Fe to Fe³⁺ valence state.

16163028,0, Downloaded from https://onlinelibrary.wilej.c.com/doi/10.1002/adfm.202306660 by University Of Texas Libraries, Wiley Online Library on [2607/2023]. See the Terms and Conditions (https://onlinelibrary.vilej.com/em-s-and-conditions) on Wiley Online Library for rules of use; OA arctices are governed by the applicable Creative Commons Licensed

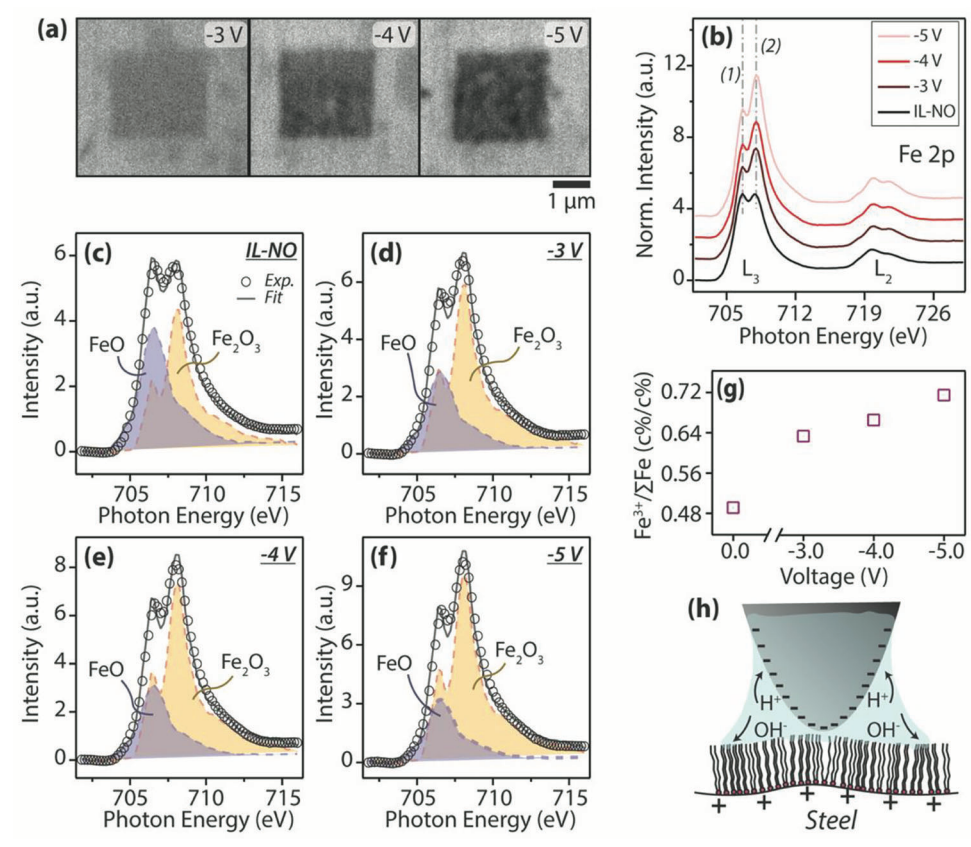


Figure 4. X-PEEM surface chemical characterization of IL-o-SPL iron oxide thin films generated using different tip biases on a $[P_{6,6,6,14}][DEHP]$ -functionalized steel surface in ambient air. a) X-PEEM images of iron oxide thin films acquired at a photon energy of 706.8 eV. b) Fe 2p XANES spectra extracted from ROIs, namely surface regions in which iron oxide layers were synthesized at different tip biases as well as the IL-NO area. The transition peaks labeled as (1) and (2) (dashed grey lines) represent split energy levels $(t_{2g} \text{ and } e_g)$ within the Fe 3d orbitals, respectively. c) Fe L₃ XANES spectra extracted from the IL-NO area and from IL-o-SPL oxide films formed at d) -3 V, e) -4 V, and f) -5 V tip bias voltage, fitted using reference Fe₂O₃ and FeO spectra. $[^{175}]$ g) Ratio of the content of Fe³⁺ to the total content of Fe obtained from the fitting results displayed in (c–f) as a function of tip voltage applied during the IL-o-SPL process. h) Schematic of the nano-cell contact where a meniscus is formed at the AFM tip/substrate interface with an applied voltage, and a $[P_{6,6,6,6,14}][DEHP]$ SAM mediates the contact.

Altogether, the XANES results demonstrate the possibility of accurately tuning the iron oxidation state on a small scale by controlling the nano-cell electrochemical reaction. In addition to Fe(II) and Fe(III) oxides, the ToF-SIMS results in Figure 3b also indicate the presence of iron oxyhydroxide (FeOOH), whose formation can provide insights into the role of ionized water during the electrolytic process. As the AFM probe is negatively biased, H⁺ ions in the water meniscus are attracted toward the AFM tip and the hydrogen evolution reaction (Reaction II in the Introduction) occurs, while OH- ions are drawn toward the water/IL interface (Figure 4h). Some of these OH⁻ contribute to the formation of FeOOH as a product of the IL-o-SPL process. However, the presence of FeOOH in the near-surface region has a minimal effect on the Fe 2p XANES spectra, as demonstrated by previous studies.^[76,77] Notably, ToF-SIMS analyses provided evidence that only a small amount of FeOOH (relative to the amounts of FeO and Fe₂O₃) was generated since the yield of FeOH⁻ fragments from the IL-o-SPL film region relative to the IL-NO background (Figure 3b) was significantly lower than the ones of FeO and Fe₂O₃. However, the formation of FeOOH is enhanced at a more negative tip voltage, as indicated by the higher contrast in

the ToF-SIMS maps of the FeOH $^-$ fragments acquired on the oxidized film generated at -5 V relative to the contrast of the same species in the maps collected on the films formed at -4 V.

2.3. Surface Potential of IL-o-SPL Oxides

To evaluate the surface potential of the oxide layers generated by IL-o-SPL, KPFM measurements were carried out together with LEEM analyses performed at the same X-PEEM/LEEM endstation as the X-PEEM experiments. **Figure 5**a shows the AFM topographic image of an oxide film formed with a tip bias of –4 V, while Figure 5b displays the corresponding surface potential map. The latter reveals that the surface potential in the IL-o-SPL oxide area is lower than the one of IL-NO by approximatively 0.1 V. Figure 5c highlights this finding by overlapping the line profiles of the surface potential and topography extracted from the blue dashed line in Figure 5b. LEEM measurements were also performed to corroborate the KPFM results. Figure 5d displays a LEEM image acquired at an electron energy of 4.1 eV on an air-oxidized steel surface functionalized by [P_{6,6,6,14}][DEHP]

16163028, 0, Downloaded from https://onlinelibrary.wiley.com/doi/10.1002/adfm.20230660 by University Of Texas Libraries, Wiley Online Library on [26/07/2023]. See the Terms and Conditions (https://onlinelibrary.wiley.com/ter

-and-conditions) on Wiley Online Library for rules of use; OA articles are governed by the applicable Creative Commons License

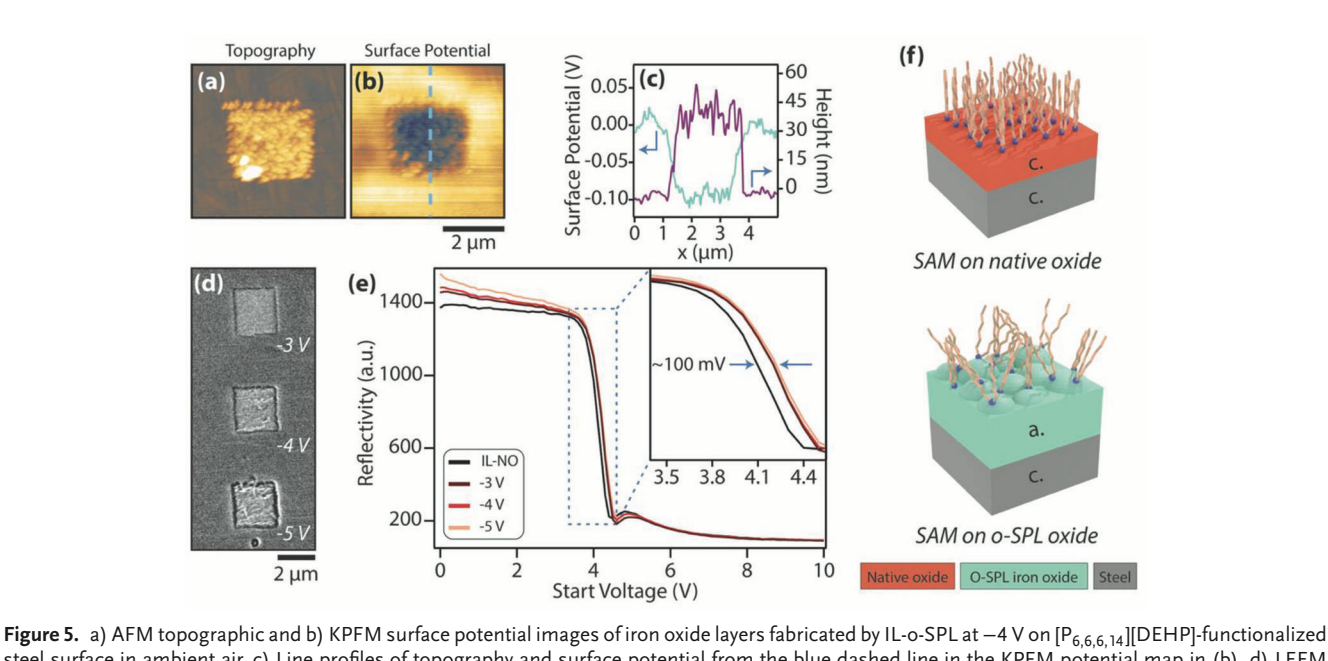


Figure 5. a) AFM topographic and b) KPFM surface potential images of iron oxide layers fabricated by IL-o-SPL at -4 V on $[P_{6,6,6,14}][\text{DEHP}]$ -functionalized steel surface in ambient air. c) Line profiles of topography and surface potential from the blue dashed line in the KPFM potential map in (b). d) LEEM image of iron oxide layers generated at different tip voltages (image acquired at 4.1 V start voltage). e) Intensity-start voltage LEEM curves extracted from ROIs. The inset spectra highlight the MEM-LEEM transition stage for surface potential comparison. f) Schematics of the proposed adsorption configurations of $[P_{6,6,6,14}][\text{DEHP}]$ SAM on native oxide/polished steel surface (upper) and IL-o-SPL iron oxide film (lower).

on which three IL-o-SPL experiments were performed at different tip bias voltages. As the LEEM images were collected while progressively changing the effective kinetic energy of the electrons impinging on the surface (referred to as "start voltage"), the intensity of the reflected/backscattered electrons reaching the detector at a certain start voltage could be extracted from different ROIs. Figure 5e displays the intensity of the back-reflected electrons as a function of the start voltage from both the IL-NO area and IL-o-SPL oxide films (usually referred to as I-V curves). At low start voltage values, the electron intensity is high as almost all electrons are reflected by the high surface electric field barrier before they can reach the sample surface - a condition usually referred to as the mirror electron microscopy (MEM) mode. As the start voltage increases, the electric field barrier becomes lower, and above a certain start voltage, the electrons have enough energy to reach the sample surface before they get backscattered (a condition usually referred to as LEEM mode), which results in a sudden drop in electron reflectivity. The transition from total electron reflection to electron backscattering, which leads to an inflection point in the I-V curve, is known as the MEM-to-LEEM transition.^[78] An increase in surface potential of a material together with an upward surface polarization leads to a shift of the inflection point in I-V measurements toward lower start voltages. [79] The I-V curves extracted from ROIs and displayed in Figure 5e indicate a higher surface potential in the IL-NO region as the inflection point is detected at a lower start voltage compared to those measured on IL-o-SPL films. This finding is consistent with the KPFM results. Notably, no significant difference could be observed in the I-V curves extracted from IL-o-SPL films, which suggests almost identical surface potentials regardless of the tip voltage used for the IL-o-SPL process. It has to be highlighted that the difference in start voltage of the inflection points for the I-V

curves extracted on IL-NO and the patterned areas is $\approx 100 \text{ mV}$ (see inset in Figure 5e), which is close to the KPFM result in Figure 5c.

Several factors should be considered to rationalize the change in surface potential of the IL-o-SPL films from the one of the as prepared steel surface (IL-NO). First, the orientation of the adsorbed $[P_{6,6,6,14}][DEHP]$ IL and the degree of structural order of the SAM-substrate complex play an important part in controlling the surface polarization, as previously demonstrated by the authors.^[80] This potential difference can thus originate from the loss of long-range order within the IL-o-SPL films shown in Figure 5f, as the adsorption configuration of SAMs is known to be closely related to the substrate crystallinity. [81,82] The two different scenarios are illustrated in Figure 2c: in the case of IL-o-SPL iron oxide films, the formation of an amorphous underlying structure disrupts the adsorption of $[P_{6,6,6,14}][DEHP]$ on steel, leading to a disoriented SAM. On the other hand, the SAM on a polished steel surface resembles a well-ordered "brush-like" structure as a result of the low surface roughness as well as the crystalline subsurface structure. [80,83] This highly ordered SAM-substrate complex exhibits higher surface polarization compared to the disoriented SAMs on the amorphous IL-o-SPL oxide films, which accounts for the distinction in surface potential between the two areas as shown by KPFM and LEEM. Regarding the chemistry of the SAMs, P 2p XANES spectra of the IL-o-SPL films of different tip voltages and the IL-NO region do not exhibit significant differences in peak shape or position (Figure S4, Supporting Information), thus indicating that the adsorbed IL maintains the same chemical structure after the IL-o-SPL process. This finding is consistent with the fact that the maximum applied voltage (-5 V) in this study is within the reported electrochemical (EC) stability window of [P_{6,6,6,14}][DEHP]. [84] In addition to the structural order of the SAM, the difference in oxide thickness between

16163028,0, Downloaded from https://onlinelibrary.wiley.com/doi/10.1002/adfm.202306660 by University Of Texas Libraries, Wiley Online Library on [26/07/2023]. See the Terms and Conditions (https://onlinelibrary.wiley.com/ems-and-conditions) on Wiley Online Library for rules of use; OA arctices are governed by the applicable Creative Commons License

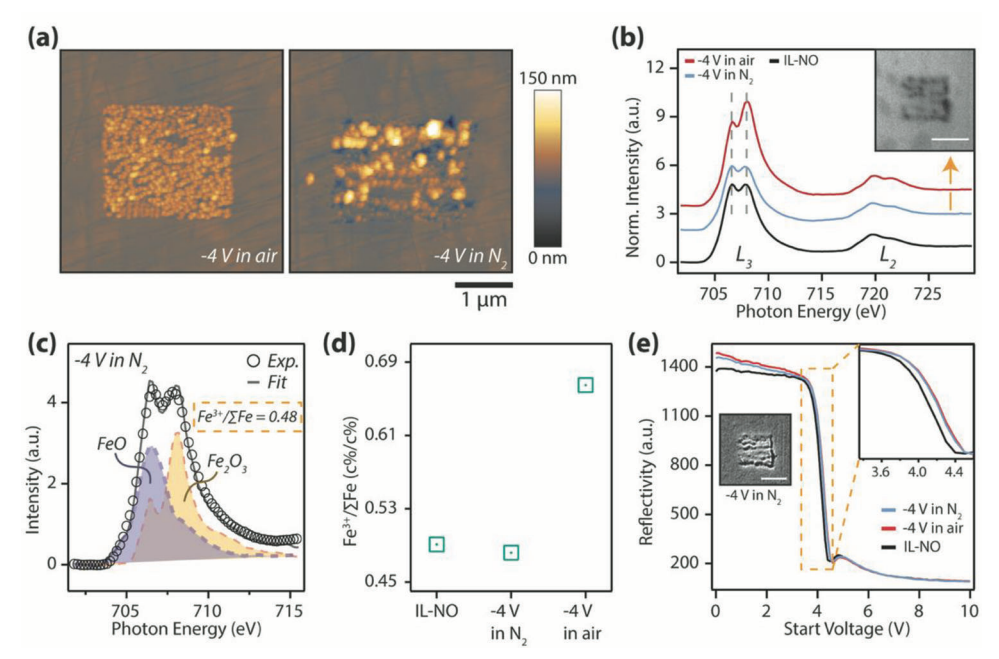


Figure 6. Atmosphere-controlled IL-o-SPL on $[P_{6,6,6,14}][DEHP]$ -functionalized steel surface. a) AFM topographic images of iron oxide films generated at -4 V in ambient air (left, high O_2 partial pressure) and N_2 (right, low O_2 partial pressure) environment. b) Fe 2p XANES spectra acquired on IL-o-SPL oxide films synthesized in air and N_2 , together with the spectrum acquired on IL-NO. The two grey dashed lines highlight the t_{2g} and e_g peaks in the L_3 edge. The inset shows the X-PEEM image of an IL-o-SPL oxide film synthesized in N_2 collected at 706.8 eV photon energy. c) Fe L_3 XANES spectrum of an IL-o-SPL oxide film synthesized at -4 V in N_2 , fitted by reference FeO and Fe $_2O_3$ spectra. $[^{75}]$ d) Fraction of iron in oxidation state +3 computed from the LCF fitting results of IL-NO and IL-o-SPL films formed in different environments. e) LEEM reflectivity spectra extracted from several ROIs. The inset spectra highlight the MEM-to-LEEM transition for surface potential comparison. The inset shows the LEEM image of an iron oxide layer generated at -4 V in N_2 , taken at a 4.1 V start voltage.

the IL-o-SPL films and IL-NO potentially contributes to their difference in surface polarization measured by KPFM and LEEM. The acquisition of LEEM data also allowed for identifying lateral variations in surface potential. Figure 5d shows that the homogeneity in surface potential decreases with the AFM tip voltage during the IL-o-SPL process, as a higher roughness of the patterned surface can lead to a corrugated surface potential profile.

2.4. Atmosphere-Control Growth of IL-o-SPL Oxides

Since o-SPL relies on the electrochemical reaction within the water meniscus formed at the point of contact between the AFM tip and the IL-functionalized steel surface, the influence of the meniscus size on the oxide island formation was investigated by performing RH-controlled IL-o-SPL experiments. In Figure 6a, the AFM topographic image of an IL-o-SPL iron oxide layer formed in N₂ (\approx 16% RH, low O₂ partial pressure) was compared to the one fabricated at the same bias, but in an ambient environment (\approx 50% RH, high O₂ partial pressure). Even though the water meniscus size decreases with the RH, the dimensions of the oxide islands formed on steel surface did not decrease when the IL-o-SPL process was performed in N2. Notably, in the case of the experiments performed in N2, the oxide islands exhibited an enhanced non-uniformity in the distribution of their dimensions and some islands had a much larger size than those formed in air. The formation of larger islands with a smaller meniscus and hence a smaller wetted area suggests that current density across the tip/substrate contact dictates the feature size, while the effect of electrowetting is secondary.

The X-PEEM characterization of the IL-o-SPL oxide film grown in N₂ provided evidence that performing the lithographic process in an environment with reduced oxygen and water partial pressure reduces the fraction of Fe in a higher oxidation state (Fe³⁺) relative to the fraction present in the films formed in air, thus suggesting that the oxidation state can be tuned by controlling the environment in which the IL-o-SPL process is carried out. Figure 6b compares the Fe 2p XANES spectrum obtained from X-PEEM measurements performed on an IL-o-SPL oxide film synthesized in N₂ with the spectrum acquired on a film grown under the same conditions, but in air, as well as the one on IL-NO. The spectrum of the oxide layer formed in N2 shows almost equal intensities of the t_{2a} and e_a peaks, which is similar to the ratio computed in the L₃ band of the IL-NO spectrum. The fitting results in Figure 6c indicate that the corresponding fraction of iron in oxidation state +3 (Fe³⁺/ Σ Fe) is 0.48, which is close to the one in the IL-NO area and much lower than the one of an IL-o-SPL oxide film synthesized in air (Figure 6d). While the oxygen and water partial pressure decrease simultaneously in an N₂ environment, their relative impacts on the oxidation of iron in the IL-o-SPL process must be considered. Previous studies on the surface oxidation of iron and iron-based alloys have shown that for both thermallyor electrochemically-grown oxides, the Fe³⁺/ \sum Fe ratio increases with the O₂ partial pressure.^[85–88] On the other hand, the presence of water has been shown to influence the rate of oxidation and corrosion in iron or iron-containing alloys, but a reduction

16163028.0, Downloaded from https://onlinelibrary.wiley.com/doi/10.1002/adfm.202306660 by University Of Texas Libraries, Wiley Online Library on [26/07/2023]. See the Terms and Conditions (https://onlinelibrary.wiley.com/doi/10.1002/adfm.202306660 by University Of Texas Libraries, Wiley Online Library on [26/07/2023]. See the Terms and Conditions (https://onlinelibrary.wiley.com/doi/10.1002/adfm.202306660 by University Of Texas Libraries, Wiley Online Library on [26/07/2023]. See the Terms and Conditions (https://onlinelibrary.wiley.com/doi/10.1002/adfm.202306660 by University Of Texas Libraries, Wiley Online Library on [26/07/2023]. See the Terms and Conditions (https://onlinelibrary.wiley.com/doi/10.1002/adfm.202306660 by University Of Texas Libraries, Wiley Online Library on [26/07/2023]. See the Terms and Conditions (https://onlinelibrary.wiley.com/doi/10.1002/adfm.202306660 by University Of Texas Libraries, Wiley Online Library on [26/07/2023]. See the Terms and Conditions (https://onlinelibrary.wiley.com/doi/10.1002/adfm.202306660 by University Of Texas Libraries, Wiley Online Library on [26/07/2023]. See the Terms and Conditions (https://onlinelibrary.wiley.com/doi/10.1002/adfm.202306660 by University Of Texas Libraries, Wiley Online Library on [26/07/2023]. See the Terms and Conditions (https://onlinelibrary.wiley.com/doi/10.1002/adfm.202306660 by University Of Texas Libraries, Wiley Online Library on [26/07/2023]. See the Texas Libraries (https://onlinelibrary.wiley.com/doi/10.1002/adfm.202306660 by University Online Library.wiley.

-and-conditions) on Wiley Online Library for rules of use; OA articles are governed by the applicable Creative Commons

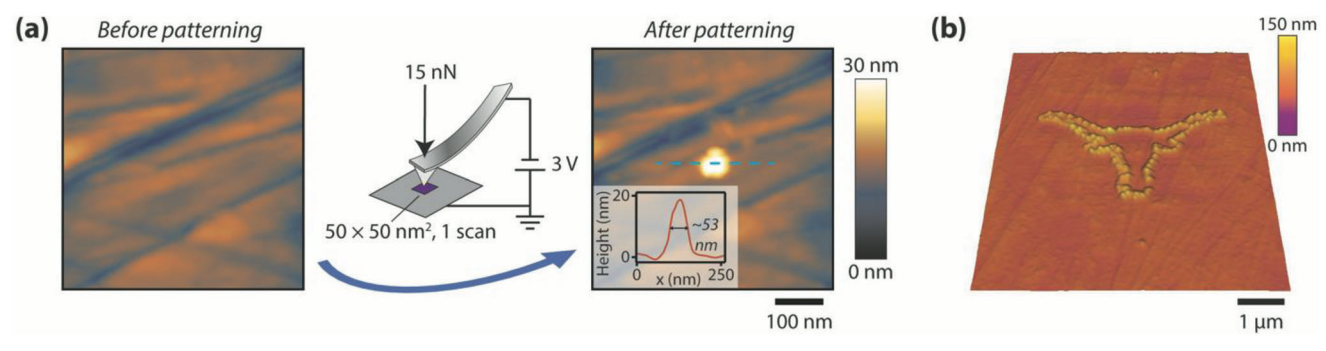


Figure 7. a) Single island formed by IL-o-SPL at -3 V on $[P_{6,6,6,14}][DEHP]$ -functionalized steel surface in an ambient environment. The scan size was set at 50×50 nm² with 256×256 pixels. The scan speed was 0.5 μm s⁻¹. Inset: line profile of height from the blue dashed line over a single island in the topographic image. b) Nanopatterned logo of the Texas Longhorns athletic team on $[P_{6,6,6,14}][DEHP]$ -functionalized steel surface with a tip bias of -4 V and a scan speed of 50 nm s⁻¹.

in water partial pressure has not been linked to any significant change in Fe³⁺/ \sum Fe ratio in the oxidized surface layers.^[89–91] Thus, the difference in Fe oxidation state detected by X-PEEM in the patterned oxide layers generated in atmosphere-control IL-o-SPL experiments is predominantly induced by variations in oxygen partial pressure. This finding sheds new light on the processes occurring during o-SPL on functionalized surfaces. Typically, metal oxidation by o-SPL without surface functionalization was described by the half-cell Reaction I (see Introduction), where only water is involved. The fact that $Fe^{3+}/\sum Fe$ varies with O2 partial pressure indicates the involvement of gaseous oxygen during iron oxidation in IL-o-SPL. In particular, oxygen (O2) molecules in the environment can result in additional cathodic and anodic reactions, namely $O_2 + 4H^+ + 4e^- \rightarrow 2H_2O$ at the cathode and $4Fe^{2+} + O_2 + 4H_2O \rightarrow 2Fe_2O_3 + 8H^+$ at the anode. The latter accounts for the increased concentration of iron in oxidation state +3 at a high O₂ partial pressure, as detected by X-PEEM.

LEEM measurements were performed to evaluate the dependence of the surface polarization of the IL-o-SPL iron oxide layers on the environment in which the lithographic process was performed. Figure 6e displays the LEEM I-V curves of oxide films synthesized in different atmospheric environments as well as in the IL-NO area. While a shift of ≈ 100 mV in MEM-LEEM transition point was detected between the I-V curves acquired on IL-NO and IL-o-SPL oxide films, the lack of any energy difference between the inflection points in the I-V curves obtained on the IL-o-SPL oxide films formed in air and N_2 indicates that these layers have similar surface potentials and that the surface polarization of IL-o-SPL films is independent of the oxide chemistry (Fe³⁺/Fe²⁺ ratio) and surface morphology (e.g., roughness and island size).

Overall, the outcomes of the experiments performed under different environmental conditions indicate that the water meniscus at the AFM tip/substrate contact provides the electrolytic nano-cell for the anodic oxidation to occur in a small area of the steel surface. The dimensions of the oxide islands are influenced by the size of the water meniscus, which strongly affects the current density across the tip/substrate contact. Notably, the localization of the electric field lines in the small water meniscus created at low RH can lead to the formation of highly non-uniform patterns (Figure 6a). Finally, the characterization of the

chemistry of the patterned areas revealed that the presence of oxygen molecules significantly influences the distribution of the oxidation state of iron. This result paves the way for performing IL-o-SPL under strictly controlled environmental conditions (not achievable with the experimental apparatus used in this study) for accurately tailoring the valence state of relevant elements in patterned layers.

2.5. IL-o-SPL for Nanolithography

To demonstrate the ability of IL-o-SPL to create complex nanostructures with good spatial resolution, two patterning experiments were performed on $[P_{6,6,6,14}][\text{DEHP}]$ -functionalized steel surfaces. In the first experiment, a single island was produced at a tip bias of -3 V (**Figure 7a**). The island has a width of $\approx\!53$ nm, which confirms the possibility of creating sub-100 nm features by IL-o-SPL.

In the second experiment, a complex nanoscale pattern was created (Figure 7b). Notably, the IL-o-SPL pattern of the logo of Texas Longhorns was generated in a single scan. This result highlights the facile patterning of oxide surface features approaching sub-100-nm dimension. However, further studies are necessary to optimize the processing parameters and precisely control feature size and shape. In fact, while the present work provided evidence that the probe voltage and the environmental RH affect the dimensions of the patterned features, extensive research is required to develop the knowledge necessary for a) tailoring the transport properties of IL adlayers by tuning the IL chemistry and structure, and b) varying the substrate nanoscale roughness with the aim of achieving high-resolution patterning.

3. Conclusions

In summary, we presented IL-o-SPL as a novel technique for patterning micro- to nano-scale oxide features on solid surfaces. The distinct IL-substrate interaction enables local oxidation at an applied bias voltage as low as $-2~\rm V$ with a simple surface functionalization procedure. Surface analyses reveal that the morphology, chemistry (e.g., fraction of iron in Fe³+ oxidation state), and surface polarization of the IL-o-SPL oxide film can be effectively controlled by tuning experimental conditions including the tip bias

16163028,0, Downloaded from https://onlinelibrary.wilej.co.ord/oi/10.1002/adfm.202306660 by University Of Texas Libraries, Wiley Online Library on [26/07/2023], See the Terms and Conditions (https://onlinelibrary.vilej.co.or/rems-and-conditions) on Wiley Online Library for rules of use; OA archies are governed by the applicable Creative Commons Licensed

voltage and atmospheric oxygen percentage. In general, IL-o-SPL brings forth several advantages compared to other lithographic techniques. For example, the method can be implemented in any standard AFMs as it operates in normal contact mode. In addition, IL-o-SPL can not only be widely accessible for singleprobe patterning on a variety of systems but also be extended to large-scale parallelization with the use of an array of AFM probes. Moreover, the short patterning time of IL-o-SPL decreases the probability of thermal or electronic drift in an AFM, thus resulting in good patterning accuracy. Among AFM-based lithographic approaches in particular, IL-o-SPL allows for highly efficient and precise patterning without the need for additional accessories (e.g., special liquid cells or sample holders) thanks to the readily formed IL EDL structure on most functional surfaces. The low applied stress used in this study can largely reduce AFM tip wear, thus increasing patterning fidelity at a high lateral resolution. Finally, the possibility of employing AFM tips with different radii of curvature and substrates with different surface chemistry provides the IL-o-SPL technique with further patterning tunability (including potentially achieving an even higher lateral resolution than the one reported here) as these parameters affect the electric field enhancement and the formation of the water meniscus. Future investigations are required to shed light on the effects of the AFM tip radius, surface roughness, and IL charge transport property on the IL-o-SPL process. Overall, the capability of IL-o-SPL to create micro- to nano-scale domains with well-controlled properties could open meaningful pathways to the development of newgeneration integrated devices, such as those based on the tunable local physical properties of multiferroic and magnetoelectric materials.

4. Experimental Section

Sample Functionalization by $[P_{6,6,6,14}][DEHP]$: $[P_{6,6,6,14}][DEHP]$ IL was synthesized using the method detailed. [80] The specimens used for AFM lithography were ASTM 52100-bearing steel (McMaster-Carr, USA). These specimens were mechanically polished (typical RMS roughness measured from a $5\times 5~\mu m^2$ area: $2.1\pm 0.4~nm)$ and stored in a desiccator for 3 days prior to the experiment. In order to functionalize the 52100 steel substrate, 0.1 mL of $[P_{6.6.6.14}][DEHP]$ IL was dropcast on the polished and air-oxidized steel surface and the sample covered by IL was placed in an ambient environment for 2 h. The specimen was then rinsed with methanol to get rid of the excessive IL and dried by N_2 , after which the $[P_{6,6,6,14}][DEHP]$ formed a SAM on the steel surface ready for AFM treatments.

IL-o-SPL: Nanoscale patterning on the functionalized surface was carried out using an MFP-3D Origin+ AFM (Oxford Instruments Asylum Research, Santa Barbara, CA, USA). To ensure the oxidation of surface materials in contact with a negatively-biased AFM probe, all functionalized steel substrates were grounded during the patterning process. Boron-doped diamond-coated conductive AFM probes (NW-CDT-FMR, NanoWorld, Switzerland) were used for the direct-write patterning procedure. In a typical patterning procedure, the AFM probe was scanned on the substrate in contact mode with a normal load of 15 nN (the average normal spring constant of the cantilevers was $6.2\ N\ m^{-1}$ according to Sader's calibration method^[92]). A negative bias (-2 V to -5 V) was applied via the conductive AFM probe during contact-mode scanning to initiate the surface oxidation. For humidity control, the AFM scanning was performed in both ambient air (\approx 50% RH) and N₂ (\approx 16% RH). The patterning was performed over a $2 \times 2 \mu m^2$ area with a biased probe in one frame, with a scan speed of 11 $\mu m\ s^{-1}$ and 256 \times 256 pixels, while for visualizing the patterned area, a $5 \times 5 \, \mu m^2$ area with the patterned site at the center was captured in tapping mode without any applied bias on the probe. The scan

speed remained the same for patterning oxide squares of other sizes. The mapping of surface electrostatic potential was obtained by KPFM. To conduct KPFM, the AFM was operated in tapping mode while scanning, using a Pt-coated probe (NSC 15/Pt, μmasch, Bulgaria). The nominal spring constant and resonance frequency of the cantilever were 40 N m⁻¹ and 325 kHz, respectively.

TEM Imaging: The extraction of a lamella from the patterned area for TEM observation was carried out using a Scios 2 DualBeam focused ion beam (FIB)/SEM system (ThermoFisher Scientific, MA, USA) with a Ga ion source. A JEOL 2010F TEM (JEOL, Japan) was used for observing the extracted cross-section and electron diffraction pattern. SEM images were taken using an FEI Quanta 650 ESEM (FEI Company, OR, USA).

X-PEEM and LEEM: X-PEEM and LEEM measurements were performed at the X-PEEM/LEEM endstation of the Electron Spectro-Microscopy (ESM) beamline (21-ID) at the National Synchrotron Light Source II (NSLS-II) located at Brookhaven National Laboratory. Both X-PEEM and LEEM measurements were performed under base pressure of $< 3 \times 10^{-10}$ Torr at room temperature. For X-PEEM, the incident X-ray was linearly polarized, with the photon energy over the span of 701.8 eV - 729.0 eV for Fe 2p (0.2 eV step size). The acquired XANES spectra were then processed by Athena for pre-edge baseline subtraction and post-edge normalization so that chemical variations between spectra can be identified. The FeO and α -Fe₂O₃ reference spectra used for fitting were previously reported. [74,75] The two reference spectra were processed the same way as the measured XANES spectra before being scaled to the same integrated intensity, a normalization procedure reported to be less sensitive to the spectral shape.^[74] In LEEM measurements, the start voltage was varied in the range of 0 V - 10 V to cover the LEEM-MEM transition with a step size of 0.1 V.

ToF-SIMS: ToF-SIMS measurements were conducted using a TOF.SIMS 5 (ION-TOF GmbH, 2010) instrument equipped with a pulsed (20 ns) Bi⁺ analysis gun (30 keV ion energy, \approx 3 pA measured sample current) and a Cs⁺ sputtering gun (0.5 keV ion energy, ≈40 nA measured sample current). The analysis ion gun was set in burst alignment (BA) mode for both high-resolution mapping and depth profiling. For chemical mapping and depth profiling over several IL-o-SPL patterned sites, a $Bi_1{}^+$ source was used as the ion beam scanned over a 45 \times 45 μm^2 area, while for mapping and depth profiling over individual IL-o-SPL films, a polyatomic Bi_3 ⁺ source was used to scan over a 15 \times 15 μm^2 area enclosing the patterned site. These acquisitions were all carried out in noninterlaced mode (i.e., sequential sputtering and analysis), with Cs⁺ sputtering to obtain the depth profiles in negative polarity. The mass resolution of the detected secondary ions was ≈ 6000 (m dm⁻¹). All measurements were performed under ultra-high vacuum conditions $(\approx 1.5 \times 10^{-9} \text{ Torr}).$

Supporting Information

Supporting Information is available from the Wiley Online Library or from the author.

Acknowledgements

The material was based upon work supported by the Welch Foundation (Grant No. F-2002-20190330 and F-2151-20230405) and the National Science Foundation Faculty Early Career Development Program (Grant No. 2042304). F.M. acknowledges support from the 2018 Ralph E. Powe Junior Faculty Enhancement Award sponsored by the Oak Ridge Associated Universities (ORAU) and from the Walker Department of Mechanical Engineering and the Texas Materials Institute at the University of Texas at Austin. This research used the synchrotron radiation facilities at the Center for Functional Nanomaterials and National Synchrotron Light Source II, U.S. Department of Energy (DOE) Office of Science User Facilities operated for the DOE Office of Science by Brookhaven National Laboratory under Contract No. DE-SC0012704.

16163028.0, Downloaded from https://onlinelibrary.wiley.com/doi/10.1002/adfm.202306660 by University Of Texas Libraries, Wiley Online Library on [26/07/2023]. See the Terms and Conditions (https://onlinelibrary.com/doi/10.1002/adfm.202306660 by University Of Texas Libraries, Wiley Online Library on [26/07/2023]. See the Terms and Conditions (https://onlinelibrary.com/doi/10.1002/adfm.202306660 by University Of Texas Libraries, Wiley Online Library on [26/07/2023]. See the Terms and Conditions (https://onlinelibrary.com/doi/10.1002/adfm.202306660 by University Of Texas Libraries, Wiley Online Library on [26/07/2023]. See the Terms and Conditions (https://onlinelibrary.com/doi/10.1002/adfm.202306660 by University Of Texas Libraries, Wiley Online Library on [26/07/2023]. See the Terms and Conditions (https://onlinelibrary.com/doi/10.1002/adfm.202306660 by University Of Texas Libraries, Wiley Online Library on [26/07/2023]. See the Terms and Conditions (https://onlinelibrary.com/doi/10.1002/adfm.20230660) by University Of Texas Libraries, Wiley Online Library on [26/07/2023]. See the Terms and Conditions (https://onlinelibrary.com/doi/10.1002/adfm.20230660) by University Of Texas Libraries, Wiley Online Library on [26/07/2023]. See the Terms and Conditions (https://onlinelibrary.com/doi/10.1002/adfm.20230660) by University Of Texas Libraries (https://onlinelibrary.com/doi/10.1002/adfm.20230660) by University Of Texas and-conditions) on Wiley Online Library for rules of use; OA articles are governed by the applicable Creative Commons

Conflict of Interest

The authors declare no conflict of interest.

Data Availability Statement

The data that support the findings of this study are available from the corresponding author upon reasonable request.

Keywords

functional oxides, ionic liquids, scanning probe lithography, surface functionalization

Received: June 12, 2023 Published online:

- M. G. Blamire, J. L. MacManus-Driscoll, N. D. Mathur, Z. H. Barber, Adv. Mater. 2009, 21, 3827.
- [2] S. C. Street, C. Xu, D. W. Goodman, Annu. Rev. Phys. Chem. 1997, 48, 43.
- [3] I. E. Wachs, Catal. Today 2005, 100, 79.
- [4] M. Chiesa, M. C. Paganini, E. Giamello, D. M. Murphy, C. Di Valentin, G. Pacchioni, Acc. Chem. Res. 2006, 39, 861.
- [5] K. Tvrdy, P. A. Frantsuzov, P. V. Kamat, Proc. Natl. Acad. Sci. U.S.A. 2011, 108, 29.
- [6] J. M. Rondinelli, N. A. Spaldin, Adv. Mater. 2011, 23, 3363.
- [7] J. Mannhart, D. G. Schlom, Science 2010, 327, 1607.
- [8] E. A. Nowadnick, J. P. Ruf, H. Park, P. D. C. King, D. G. Schlom, K. M. Shen, A. J. Millis, *Phys. Rev. B* 2015, 92, 245109.
- [9] J. Mravlje, M. Aichhorn, T. Miyake, K. Haule, G. Kotliar, A. Georges, Phys. Rev. Lett. 2011, 106, 096401.
- [10] J. M. Rondinelli, N. M. Caffrey, S. Sanvito, N. A. Spaldin, Phys. Rev. B 2008, 78, 155107.
- [11] M. Imada, A. Fujimori, Y. Tokura, Rev. Mod. Phys. 1998, 70, 1039.
- [12] E. Roduner, Chem. Soc. Rev. 2006, 35, 583.
- [13] P. Yang, C. M. Lieber, Science 1996, 273, 1836.
- [14] J. Dho, X. Qi, H. Kim, J. L. MacManus-Driscoll, M. G. Blamire, Adv. Mater. 2006, 18, 1445.
- [15] A. Dey, M. K. Nayak, A. C. M. Esther, M. S. Pradeepkumar, D. Porwal, A. K. Gupta, P. Bera, H. C. Barshilia, A. K. Mukhopadhyay, A. K. Pandey, K. Khan, M. Bhattacharya, D. R. Kumar, N. Sridhara, A. K. Sharma, Sci. Rep. 2016, 6, 36811.
- [16] D. Mukherjee, A. Dey, A. C. M. Esther, D. Palai, N. Sridhara, P. Bera, M. Bhattacharya, A. Rajendra, A. K. Sharma, A. K. Mukhopadhyay, Ceram. Int. 2018, 44, 8913.
- [17] J. Zhang, Y. Wang, H. Ji, Y. Wei, N. Wu, B. Zuo, Q. Wang, J. Catal. 2005, 229, 114.
- [18] O. Shekhah, W. Ranke, A. Schüle, G. Kolios, R. Schlögl, Angew. Chem. Int. Ed. 2003, 42, 5760.
- [19] X. Cui, C. Tang, X.-M. Liu, C. Wang, W. Ma, Q. Zhang, Chem. Eur. J. 2018, 24, 18494.
- [20] K. Široký, J. Jirešová, L. Hudec, Thin Solid Films 1994, 245, 211.
- [21] J. Chen, L. Xu, W. Li, X. Gou, Adv. Mater. 2005, 17, 582.
- [22] L. Lartigue, C. Wilhelm, J. Servais, C. Factor, A. Dencausse, J.-C. Bacri, N. Luciani, F. Gazeau, ACS Nano 2012, 6, 2665.
- [23] C. J. Belle, A. Bonamin, U. Simon, J. Santoyo-Salazar, M. Pauly, S. Bégin-Colin, G. Pourroy, Sens. Actuators B Chem. 2011, 160, 942.
- [24] P. Li, D. E. Miser, S. Rabiei, R. T. Yadav, M. R. Hajaligol, Appl. Catal. B 2003, 43, 151.
- [25] R. Wu, J. Qu, Y. Chen, Water Res. 2005, 39, 630.

- [26] R. Chalasani, S. Vasudevan, J. Mater. Chem. 2012, 22, 14925.
- [27] M. Gich, I. Fina, A. Morelli, F. Sánchez, M. Alexe, J. Gàzquez, J. Fontcuberta, A. Roig, Adv. Mater. 2014, 26, 4645.
- [28] E. H. Abdelhamid, O. D. Jayakumar, V. Kotari, B. P. Mandal, R. Rao, V. M. Naik, R. Naik, A. K. Tyagi, RSC Adv. 2016, 6, 20089.
- [29] S. Ramazanov, D. Sobola, Ş. Ţălu, F. Orudzev, A. Arman, P. Kaspar, R. Dallaev, G. Ramazanov, Microsc. Res. Tech. 2022, 85, 1300.
- [30] I. Khan, A. Khalil, F. Khanday, A. M. Shemsi, A. Qurashi, K. S. Siddiqui, Arab. J. Sci. Eng. 2018, 43, 43.
- [31] G. R. Patzke, Y. Zhou, R. Kontic, F. Conrad, Angew. Chem. Int. Ed. 2011, 50, 826.
- [32] L.-S. Zhong, J.-S. Hu, H.-P. Liang, A.-M. Cao, W.-G. Song, L.-J. Wan, Adv. Mater. 2006, 18, 2426.
- [33] B. L. Cushing, V. L. Kolesnichenko, C. J. O'Connor, Chem. Rev. 2004, 104, 3893.
- [34] M. Yoshimura, K. Byrappa, J. Mater. Sci. 2008, 43, 2085.
- [35] M. Cargnello, T. R. Gordon, C. B. Murray, Chem. Rev. 2014, 114, 9319.
- [36] B. P. Isaacoff, K. A. Brown, Nano Lett. 2017, 17, 6508.
- [37] Y. A. Diaz Fernandez, T. A. Gschneidtner, C. Wadell, L. H. Fornander, S. L. Avila, C. Langhammer, F. Westerlund, K. Moth-Poulsen, *Nanoscale* 2014, 6, 14605.
- [38] M. Zhang, D. J. Magagnosc, I. Liberal, Y. Yu, H. Yun, H. Yang, Y. Wu, J. Guo, W. Chen, Y. J. Shin, A. Stein, J. M. Kikkawa, N. Engheta, D. S. Gianola, C. B. Murray, C. R. Kagan, Nat. Nanotechnol. 2017, 12, 228.
- [39] S. Sharma, S. S. Pande, P. Swaminathan, RSC Adv. 2017, 7, 39411.
- [40] P. Fan, M. Zhong, B. Bai, G. Jin, H. Zhang, RSC Adv. 2016, 6, 45923.
- [41] R. Garcia, A. W. Knoll, E. Riedo, Nat. Nanotechnol. 2014, 9, 577.
- [42] R. D. Piner, J. Zhu, F. Xu, S. Hong, C. A. Mirkin, Science 1999, 283, 661
- [43] J. Chai, F. Huo, Z. Zheng, L. R. Giam, W. Shim, C. A. Mirkin, Proc. Natl. Acad. Sci. U.S.A. 2010, 107, 20202.
- [44] L. Weng, L. Zhang, Y. P. Chen, L. P. Rokhinson, Appl. Phys. Lett. 2008, 93, 093107.
- [45] A. A. Tseng, Small 2011, 7, 3409.
- [46] M. Holz, F. I. Allen, C. Reuter, A. Ahmad, M. Hofmann, A. Reum, T. Ivanov, I. W. Rangelow, J. Vac. Sci. Technol. B 2019, 37, 061812.
- [47] Y. K. Ryu, R. Garcia, Nanotechnology 2017, 28, 142003.
- [48] D. Wouters, S. Hoeppener, U. S. Schubert, Angew. Chem. Int. Ed. 2009, 48, 1732.
- [49] H. Sugimura, N. Nakagiri, Jpn. J. Appl. Phys. 1995, 34, 3406.
- [50] Y. Li, B. Maynor, J. Liu, J. Am. Chem. Soc. 2001, 123, 2105.
- [51] B. Kim, G. Pyrgiotakis, J. Sauers, W. M. Sigmund, Colloids Surf. A Physicochem. Eng. Asp. 2005, 253, 23.
- [52] J. Park, H. Lee, Mater. Sci. Eng. C 2004, 24, 311.
- [53] R. Garcia, R. V. Martinez, J. Martinez, Chem. Soc. Rev. 2006, 35, 29.
- [54] D. Meroni, S. Ardizzone, U. S. Schubert, S. Hoeppener, Adv. Funct. Mater. 2012, 22, 4376.
- [55] T. Welton, Chem. Rev. 1999, 99, 2071.
- [56] C. Verma, E. E. Ebenso, M. A. Quraishi, J. Mol. Liq. 2017, 233, 403.
- [57] J. Cole, K. L. Syres, J. Phys. Condens. Matter 2022, 34, 213002.
- [58] O.-P. Li, B. Yan, RSC Adv. 2012, 2, 10840.
- [59] M. Shakourian-Fard, S. Maryamdokht Taimoory, V. Semeniuchenko, G. Kamath, J. F. Trant, J. Mol. Liq. 2018, 268, 206.
- [60] R. Atkin, G. G. Warr, J. Phys. Chem. C 2007, 111, 5162.
- [61] D. S. Silvester, R. Jamil, S. Doblinger, Y. Zhang, R. Atkin, H. Li, J. Phys. Chem. C 2021, 125, 13707.
- [62] M. V. Fedorov, A. A. Kornyshev, Chem. Rev. 2014, 114, 2978.
- [63] M. Galiński, A. Lewandowski, I. Stepniak, *Electrochim. Acta* 2006, 51,
- [64] G. Yang, X. Lu, Y. Bai, H. Cui, Z. Jin, J. Alloys Compd. 2002, 345, 196.

16163028,0, Downloaded from https://onlinelibrary.wiley.com/doi/10.1002/adfm.202306660 by University Of Texas Libraries, Wiley Online Library on [26/07/2023]. See the Terms

on Wiley Online Library for rules of

use; OA articles

are governed by the applicable Creative Commons

- [65] X. Wu, P. Su, Z. Jiang, S. Meng, ACS Appl. Mater. Interfaces 2010, 2, 808. 14194.
- [66] J.-H. Kim, J.-H. Lee, A. Mirzaei, H. W. Kim, B. T. Tan, P. Wu, S. S. Kim, Sci. Rep. 2020, 10, 14194.
- [67] A. Prasad, N. V. Salim, M. Mozetič, L. Kailas, S. Thomas, J. Appl. Polym. Sci. 2022, 139, 52286.
- [68] P. Pedeferri, Corrosion Science and Engineering (Eds.: L. Lazzari, M. Pedeferri), Springer, Cham, 2018.
- [69] P. A. van Aken, S. Lauterbach, Phys. Chem. Miner. 2003, 30, 469.
- [70] W. C. Wang, S. Y. Chen, P. A. Glans, J. Guo, R. J. Chen, K. W. Fong, C. L. Chen, A. Gloter, C. L. Chang, T. S. Chan, J. M. Chen, J. F. Lee, C. L. Dong, *Phys. Chem. Chem. Phys.* **2013**, *15*, 14701.
- [71] Sarveena, J. M. Vargas, D. K. Shukla, C. T. Meneses, P. Mendoza Zélis, M. Singh, S. K. Sharma, Phys. Chem. Chem. Phys. 2016, 18, 9561
- [72] W. S. Chang, C.-S. Tu, P.-Y. Chen, C.-S. Chen, C.-Y. Lin, K.-C. Feng, Y. L. Hsieh, Y. H. Huang, J. Alloys Compd. 2017, 710, 670.
- [73] P. S. Miedema, F. M. F. de Groot, J. Electron Spectros. Relat. Phenom. 2013. 187, 32.
- [74] T. J. Regan, H. Ohldag, C. Stamm, F. Nolting, J. Lüning, J. Stöhr, R. L. White, *Phys. Rev. B* 2001, 64, 214422.
- [75] S. W. Han, J. S. Kang, S. S. Lee, G. Kim, S. J. Kim, C. S. Kim, J. Y. Kim, H. J. Shin, K. H. Kim, J. I. Jeong, B. G. Park, J. H. Park, B. I. Min, J. Phys. Conden. Matter 2006, 18, 7413.
- [76] B. P. von der Heyden, A. N. Roychoudhury, T. Tyliszczak, S. C. B. Myneni, Am. Mineral. 2017, 102, 674.
- [77] S.-Y. Chen, A. Gloter, A. Zobelli, L. Wang, C.-H. Chen, C. Colliex, Phys. Rev. B 2009, 79, 104103.

- [78] N. Barrett, J. E. Rault, J. L. Wang, C. Mathieu, A. Locatelli, T. O. Mentes, M. A. Niño, S. Fusil, M. Bibes, A. Barthélémy, D. Sando, W. Ren, S. Prosandeev, L. Bellaiche, B. Vilquin, A. Petraru, I. P. Krug, C. M. Schneider, J. Appl. Phys. 2013, 113, 187217.
- [79] G. F. Nataf, P. Grysan, M. Guennou, J. Kreisel, D. Martinotti, C. L. Rountree, C. Mathieu, N. Barrett, Sci. Rep. 2016, 6, 33098.
- [80] Z. Li, A. Dolocan, O. Morales-Collazo, J. T. Sadowski, H. Celio, R. Chrostowski, J. F. Brennecke, F. Mangolini, Adv. Mater. Interfaces 2020, 7, 2000426.
- [81] M. J. Brukman, G. Oncins, T. D. Dunbar, L. D. Boardman, R. W. Carpick, Langmuir 2006, 22, 3988.
- [82] P. Thissen, M. Valtiner, G. Grundmeier, Langmuir 2010, 26, 156.
- [83] Z. Li, O. Morales-Collazo, R. Chrostowski, J. F. Brennecke, F. Mangolini, RSC Adv. 2022, 12, 413.
- [84] F. Gatti, T. Amann, A. Kailer, N. Baltes, J. Rühe, P. Gumbsch, Sci. Rep. 2020, 10, 17634.
- [85] E. Essuman, G. H. Meier, J. Żurek, M. Hänsel, W. J. Quadakkers, Oxid. Met. 2008, 69, 143.
- [86] D. Klimm, S. Ganschow, J. Cryst. Growth 2005, 275, e849.
- [87] J. Wiencke, H. Lavelaine, P.-J. Panteix, C. Petitjean, C. Rapin, J. Appl. Electrochem. 2018, 48, 115.
- [88] M. Muller, H. El-Rabii, R. Fabbro, J. Mater. Sci. 2015, 50, 3337.
- [89] N. Bertrand, C. Desgranges, D. Poquillon, M. C. Lafont, D. Monceau, Oxid. Met. 2010, 73, 139.
- [90] J. Shen, L. Zhou, T. Li, Oxid. Met. 1997, 48, 347.
- [91] J. Chen, Z. Shen, J. Zhang, High Temp. Corrosion Mater. 2023, 99, 15.
- [92] J. E. Sader, J. W. M. Chon, P. Mulvaney, Rev. Sci. Instrum. 1999, 70, 3967.